Experimental Investigation of Shock-Induced Tandem Droplet Breakup

Zhaoguang Wang (王召光)*, Thomas Hopfes, Marcus Giglmaier, Nikolaus A. Adams
Chair of Aerodynamics and Fluid Mechanics, Technical University of Munich, 85748 Garching, Germany
* *Corresponding author: zg.wang@tum.de*

Abstract
For deeper insights into the dynamics of dense sprays, the present experimental work investigates the shock-induced breakup of two identically-sized water droplets in tandem formation. The breakup process is visualized in a shadowgraph system and captured by an ultra-high-speed camera. The experimental Weber number ranges from 13 to 180 and the separation distance between droplets is varied between 1.2 and 10.5 times of the droplet diameter. While the tandem formation exerts marginal influence on the lead droplet, the breakup intensity of the trailing droplet is consistently attenuated as the separation distance falls below critical levels. The time of initial deformation is postponed, the maximum cross-stream diameter is reduced, and the mean drag coefficient is lowered. These effects are more profound at lower Weber numbers and closer separation distances. The attenuation of the breakup intensity is also reflected by the formation of smaller bags in bag and bag-and-stamen morphologies and by the narrower cross-stream dispersion of fragments in multibag and shear stripping morphologies. When positioned in close proximity to the lead droplet, the trailing droplet fails to follow the conventional breakup morphologies. Instead, it either punctures or coalesces with the lead droplet.

Keywords: droplet breakup; tandem formation; dense spray; secondary atomization

1 Introduction

Droplet breakup is a relevant phenomenon in a variety of applications, including fuel injection (Reitz and Diwakar 1986), powder metallurgy (Lagutkin et al. 2004) and spray coatings (Mostaghimi et al. 2002). Previous research has concluded that the droplet breakup process is mainly governed by the Weber number (*We*) and the Ohnesorge number (*Oh*) (Lane 1951; Hinze 1955)

$$We = \rho_g u_g^2 d_0/\sigma \qquad \textbf{(Eqn. 1)}$$

$$Oh = \mu_d/\sqrt{\rho_d d_0 \sigma} \qquad \textbf{(Eqn. 2)}$$

where ρ_g and u_g are the density and the velocity of the gas flow, and d_0, σ, μ_d and ρ_d are the initial diameter, the surface tension, the dynamic viscosity and the density of the liquid droplet. The Weber number and the Ohnesorge number compare the disruptive aerodynamic force and the viscous force against the restorative surface tension, respectively. When $Oh < 0.1$, the significance of the liquid viscosity becomes negligible and *We* turns to be the solely dominant factor (Guildenbecher, López-Rivera, and Sojka 2009).

The aerodynamic breakup of single droplets has been extensively investigated and reviewed in detail by Pilch and Erdman (1987), Faeth et al. (1995) and Guildenbecher et al. (2009). As the aerodynamic force becomes increasingly intense, the corresponding breakup pattern transitions from bag breakup (Chou and Faeth 1998; Joseph, Belanger, and Beavers 1999; Han and Tryggvason 1999) to stripping breakup (Ranger and Nicholls 1969; Z. Liu and Reitz 1997; Theofanous and Li 2008). There exist several in-between multimode morphologies (Dai and Faeth 2001; Chen et al. 2017), and the two covered in the current work are bag-and-stamen breakup (Pilch and Erdman 1987; Hsiang and Faeth 1992) and multibag breakup (Theofanous, Li, and Dinh 2004; Jain et al. 2015).

However, the conventional understandings of single droplet breakup do not describe the breakup behavior in dense sprays accurately. In practical applications such as diesel injections (Ashgriz 2011) and agricultural sprays (Dorr et al. 2013), droplets appear in close proximity instead of being isolated. The interaction between adjacent droplets has to be considered to properly estimate the fragment sizes. Therefore, the arrangement of droplets in tandem formation is more representative than single droplets and the initial on-center separation distance *s* between the tandem droplets becomes an additional variable of importance. The associated tandem breakup behavior is investigated thoroughly in the current work.

Most of the previous research about droplets in tandem formation is dedicated to the evaluation of drag coefficients. Liu et al. (1988) study experimentally the laminar flow field around an infinite droplet chain with the normalized on-center separation distance $S = s/d_0$ varied between 2 and 12. They conclude that the drag coefficient of monodisperse droplets is up to an order of magnitude lower than the drag coefficient of isolated droplets. Mulholland et al. (1988) conduct similar experiments but with *S* ranging from 1.7 to 1700. They propose an empirical formulation to model the drag coefficient and find that the value is significantly diminished as the separation distance drops below 150. Poo and Ashgriz (1991) investigate a stream of closely spaced droplets with $S < 5$ in a turbulent flow and state that the drag coefficient is 4 to 5 times smaller compared to isolated droplets. There are other studies with the focus on a finite number of droplets in tandem formation instead of an infinite stream. Temkin and Ecker (1989) study the interaction between two droplets with *S* from 1.5 to 11 and Reynolds numbers below 150. Based on the quantified changes of drag coefficients, they show that the upstream droplet is not affected by the tandem formation while the downstream one experiences reduction up to 50%. The result also suggests that the region of influence behind the upstream droplet extends over 15 droplet diameters. Nguyen and Dunn-Rankin (1992) examine vertically falling droplet packets composed of 4 droplets separated by 5.5 diameters with the Reynolds number around 80. They analyze the trajectory of the first trailing droplet and present that the drag coefficient is 25% lower than that of the lead droplet. Chiang and Sirignano (1993) investigate numerically the transportation of three droplets aligned with the flow direction. Their results indicate that the drag of the first two droplets differs profoundly while the difference between the downstream two droplets becomes insignificant.

The amount of research focusing on the deformation and breakup of tandem droplets is very limited, among which the experimental work is even scarcer. Zhao et al. (2019) conduct experiments of two neighboring droplets at $We = 12.3$ in the bag breakup regime with the normalized separation distance *S* below 3. For cases with the two droplets positioned in tandem, they report a coalescence mode at $S < 1.3$ and a puncture mode at higher *S*. Igra and Takayama (2003) experimentally investigate the shear stripping breakup of two water columns

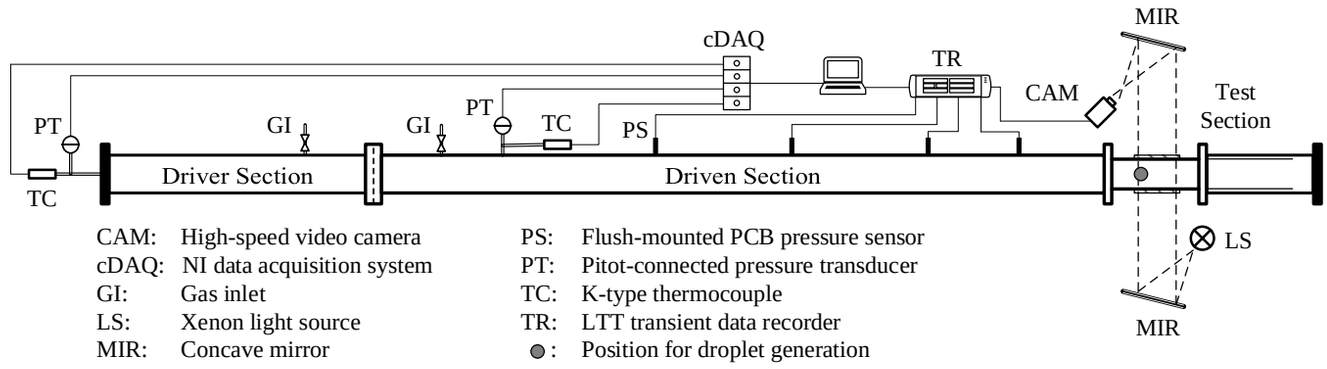

Fig. 1. Layout of the shock tube and the measurement system.

separated 5 diameters away at the Weber number of 6900. The same breakup behavior as single columns is observed for the front column while the rear one deforms at a much lower rate. Others adopt numerical methods for the relevant research. Quan et al. (2011) employ a finite-volume scheme to investigate the deformation of tandem droplets spaced within 6 diameters at Weber numbers of 40, 4 and 0.4. They present a mushroom shape formed by the droplet pair at the two largest Weber numbers with $S = 1.6$. Simulations of similar tandem arrangements are carried out by Kékesi et al. (2019), with the Weber number of 20 and the separation distance from 1.5 to 5 droplet diameters. They conclude that the trailing droplet either shoots through or merges with the lead droplet and its breakup time is increased significantly. Stefanitsis et al. (2019) apply the Volume of Fluid method to study the breakup of four diesel droplets in tandem formation at Weber numbers varied between 15 and 64. They analyze the deformation of the third droplet and present a new breakup mode termed as shuttlecock. Their results show that the interaction between tandem droplets becomes important for separation distances below 9 droplet diameters.

To shed more light on the breakup features of tandem droplets, the current experimental work intends to assess the significance of the tandem formation over a wide range of Weber numbers and separation distances. In contrast to most of the previous works that focus on the evaluation of drag reduction, we place emphasis on detailed description of deformation patterns and breakup structures. The present results can serve as bases for potential numerical validations and for more accurate modelling of fragment sizes and dispersion.

2 Experimental Setup

The layout of the shock tube and the measurement system employed in the present work is provided in Fig. 1. The setup is the same as described in our previous work (Wang et al. 2020), except for the position of the cookie-cutter. The square cookie-cutter, which conventionally locates upstream of the test section to remove boundary layers, is shifted downstream to achieve a longer period of steady flow conditions. Fig. 2 sketches the propagation of the incident shock inside the tube, and Fig. 3 plots the corresponding post-shock pressure at the test point measured by PCB Piezotronics ICP® fast-response pressure sensors. When reaching the front of the test section, the incident shock partially reflects since the cross section contracts to a 190 × 190 mm^2 square (t = -0.5 ms in Fig. 2). The reflected shock leads to a short transition period (~0.2 ms), after the pressure at the test location experiences a stepwise increase at the arrival of the incident shock (t = 0 ms in Fig. 3). As the incident shock exits from the test section, the increase of the cross section area induces generation of additional expansion waves (t = 2.2 ms in Fig. 2). These expansion waves propagate upstream and give rise to pressure drop and velocity increase at the test location (t = 4.5 ms in Fig. 3). By shifting the cookie-cutter to the downstream of the test section, the upstream propagation of the expansion waves is postponed and thus the steady-flow time window is prolonged from ~2 ms in the previous setup (Wang et al. 2020) to ~4.5 ms, at the expense of causing a short transition period and slightly higher flow fluctuations.

In the current work, the steady-flow period covers the entire breakup process of cases at high Weber numbers. For cases at the two lowest Weber numbers (We = 13 and 24), the early-stage deformation and the initiation of bag development are within the steady-flow period but the onset of bag rupture is beyond. Nevertheless, although the timing for the bag rupture is altered by the changing flow conditions, the main deformation patterns are preserved for these cases. Particularly, the early-stage parameters quantified in Section 3.5 are not affected.

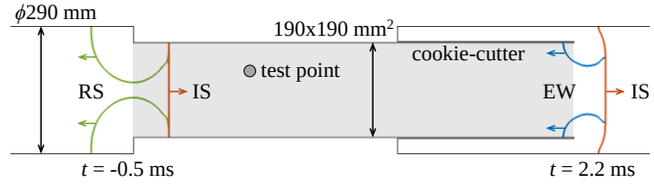

Fig. 2. Wave dynamics inside the test section. The test section is marked with gray shades. The incident shock propagates from left to right. (IS: incident shock, RS: reflected shock, EW: expansion wave).

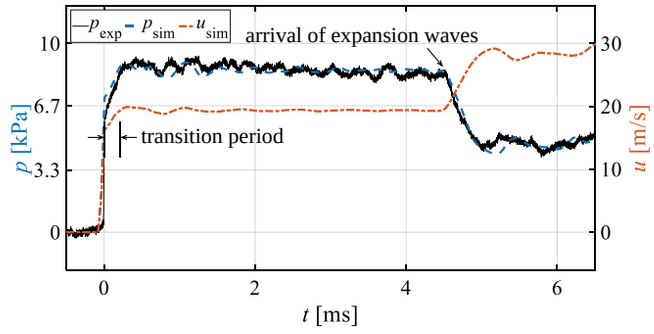

Fig. 3. Post-shock flow pressure and velocity at the test point (We = 13).

In the current experiments, the velocity of the incident shock is calculated by measuring the time difference between moments when the incident shock passes two 0.75 m-separated

pressure sensors directly upstream of the test section. Based on this shock speed and the initial atmospheric conditions, we conduct 2D axisymmetric numerical simulations to estimate post-shock flow parameters. As shown in Fig. 3, the simulated pressure profile at the test point is in good agreement with that measured experimentally. This justifies the application of the flow velocity and density obtained from the numerical simulation in the calculation of Weber numbers.

In terms of flow visualization, shadowgraph images of the droplet breakup are recorded by a Shimadzu HyperVision HPV-X ultra-high-speed camera at framing rates of 10 – 40 kfps. The images are processed with background subtraction, contrast adjustment and super resolution using MATLAB's Very Deep Super-Resolution convolutional neural network (Kim et al. 2016). The spatial resolution of the resultant images is ~0.05 mm/pixel. By counting the pixels that constitute the droplet in the shadowgraph image the cross-sectional area A is obtained, and the equivalent droplet diameter d_0 is calculated as $d_0 = 2\times(A/\pi)^{0.5}$.

Table 1. Operating flow conditions summarized from repeated experiments.

We	Oh_{avg}	$Re_{\infty avg}$	breakup morphology
13 (±1.3)	2.4e-3	2.5e3	bag breakup
24 (±2.2)	2.4e-3	3.4e3	bag and stamen
70 (±3.0)	2.3e-3	6.1e3	multibag breakup
180 (±10)	2.4e-3	1.0e4	shear stripping

To generate droplets in tandem formation, two syringe needles separated with a defined spacing are inserted into the test section. After droplets with the diameter of ~2 mm are produced at the needle tips, the syringes are withdrawn rapidly detaching the two droplets simultaneously. The current experimental matrix covers four flow conditions, of which the parameters are summarized in Table 1 based on repeated experiments. The average Weber numbers investigated are 13, 24, 70 and 180, with the corresponding breakup morphology changing from bag breakup to shear stripping. The Ohnesorge number for all cases is approximately 2.4e-3, making the viscous effect negligible (Guildenbecher, López-Rivera, and Sojka 2009). The d_0-based freestream Reynolds number Re_∞

$$Re_\infty = \rho_g u_g d_0/\mu_g \qquad \textbf{(Eqn. 3)}$$

increases from 2.5e3 to 1.0e4. Under each flow condition, seven on-center separation distances $S = s/d_0$ between 1.2 and 10.5 are studied. In addition, single droplet experiments are conducted as well for more comprehensive comparisons.

3 Results and Discussion

In the current study, the experiment time t is normalized against the characteristic transport time derived by Ranger and Nicholls (1969) to yield the non-dimensional time T:

$$T = t \cdot u_g / (d_0\sqrt{\rho_d/\rho_g}). \qquad \textbf{(Eqn. 4)}$$

The time for lead and trailing droplets is zeroed at the instant of the incident shock impacting on their respective frontal surface. Nevertheless, the time shift between the tandem droplets is less than 0.06 ms for all cases and insignificant compared to the duration of breakup process at current conditions. For the sake of consistency and brevity, only the time for the lead droplet is provided in the following image sequences. As presented in Fig. 3, the freestream flow condition remains steady until t = 4.5 ms. The corresponding non-dimensional time instants are approximately T = 1.7, 2.2, 3.6 and 6.0 for current experiments at Weber numbers of 13, 24, 70 and 180, respectively. The breakup process is completed under constant flow conditions for high Weber numbers, but slightly exceeds the steady-flow period for low Weber numbers. In the following texts, time instants that exceed this period are marked with T* instead of T.

Fig. 4 provides an overview of the interactive modes between the tandem droplets. Considering that the lead droplet breakup is marginally influenced by the tandem formation, Fig. 4 only categorizes the change of the breakup pattern for the trailing droplet at different separation distances S and Weber numbers *We*. In the figure, the x-axis S is plotted on the linear scale and the y-axis *We* on the logarithmic scale. The entire *S*-*We* map is divided into three regions. The independent breakup region at the top-right corner represents cases where the trailing droplet undergoes the same breakup process as the lead droplet. The suppressed breakup region at the bottom-left corner contains cases where the trailing droplet fails to follow the breakup morphology of the lead droplet but exhibits either puncture or coalescence modes instead. For cases in the transition region, the breakup morphology of the trailing droplet is the same as that of the lead droplet but the breakup intensity is reduced. The boundary between the independent breakup region and the transition region is of particular importance, because it represents the critical separation distance below which the interaction of the tandem droplets has to be taken into account. This critical distance is *We*-dependent and halved from S = 10.8 at *We* = 13 to S = 5.4 at *We* = 180.

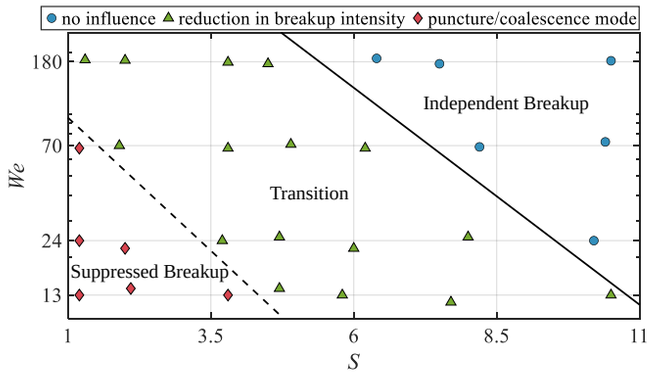

Fig. 4. Change of the breakup pattern of the trailing droplet at different separation distances and Weber numbers, in comparison to the lead droplet. The map is divided into three regions (independent breakup region, transition region and suppressed breakup region).

The following presentation of results starts with illustrating the breakup pattern of the tandem droplets with shadowgraph images for each breakup morphology individually (Section 3.1 – 3.4). In each section, representative cases at a certain Weber number in the transition and the suppressed breakup regions are described in detail while those in the independent breakup region are omitted for conciseness. The discussion is concluded by quantifying the time of initial deformation, the maximum cross-stream diameter and the mean drag coefficient of the tandem droplets in Section 3.5.

3.1 Bag breakup

3.1.1 Transition region: smaller bag for the trailing droplet

For the bag breakup of tandem droplets, the present cases with separation distances between 4.7 and 10.5 are identified in the transition region. An exemplary case is shown in Fig. 5 with S = 5.8 and *We* = 13. Here, the lead droplet replicates the breakup process of single droplets and experiences initial flattening (T = 1.0), bag inflation (T = 1.5), bag rupture

(T^* = 2.35) and ring disintegration (T^* = 2.8) sequentially. The trailing droplet exhibits the same breakup morphology as the lead droplet, but is flattened to a lower cross-stream diameter (d_c) in the early stage and develops a smaller bag at a later time. In all following figures that present breakup structures, the explanatory notes on the right describe the breakup progress of the trailing droplet.

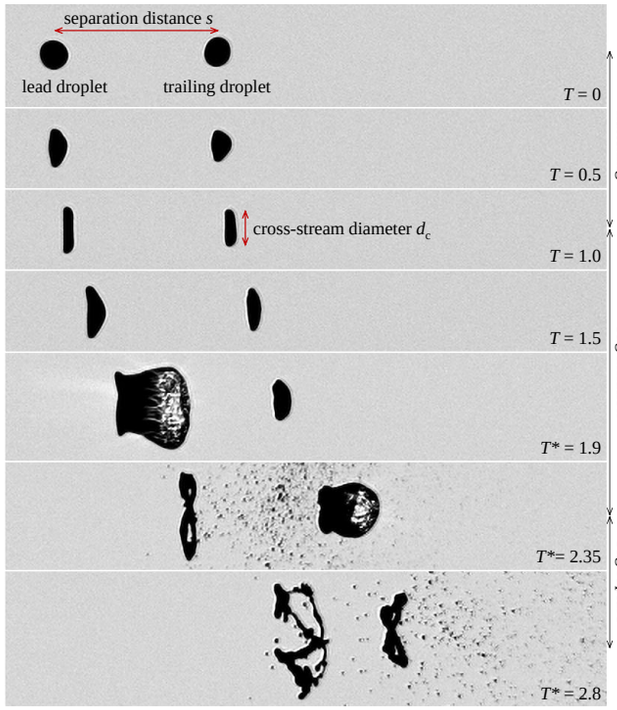

Fig. 5. Weaker flattening and smaller bag size for the trailing droplet under the shielding effect of the lead droplet (S = 5.8, We = 13). The freestream direction is from left to right for all presented images. As labelled, s and d_c are the initial on-center separation distance and the cross-stream diameter, respectively.

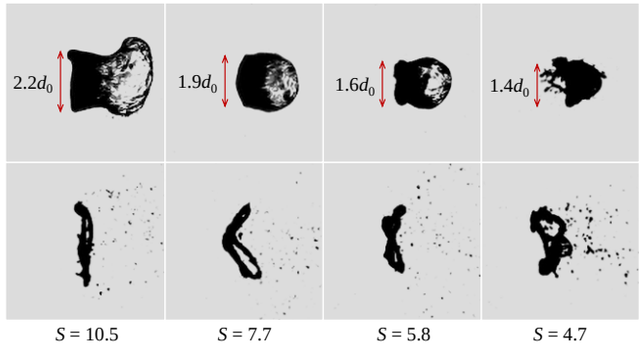

Fig. 6. Variation of the bag size and the ring thickness at different separation distances for the trailing droplet in the bag breakup regime. The top and bottom rows correspond to time instants prior and subsequent to the bag rupture, respectively. (We = 13, 12, 13 and 15 from left to right).

As demonstrated by the top row in Fig. 6, the main variation within the transition region is that the bag formed by the trailing droplet becomes consistently smaller as the separation distance decreases. The reduction of the bag size is associated with the less pronounced flattening in the early stage and results from the fact that the wake flow of the lead droplet shields the trailing droplet and lowers the pressure imposed on its windward surface. This shielding effect is stronger at closer separation distances. The bottom row in Fig. 6 compares the ring structure of the trailing droplet after fragmentation of the bag. On the one hand, smaller bags mean that less mass is shed off through the bag rupture and more remains in the toroidal ring. On the other hand, the bag size also determines the diameter of the ring in a proportional way. Consequently, under the combined influence of these two factors, the ring is thickened when the trailing droplet is in closer proximity to the lead droplet. Although the time instants shown in Fig. 6 are beyond the steady-flow period, all cases still share approximately the same flow conditions and thus the tendency presented here remains valid qualitatively.

3.1.2 Suppressed breakup region: puncture of the lead droplet by the trailing droplet

The interaction of the tandem droplets at separation distances S = 2.1 and 3.8 are identified as the puncture mode in the suppressed breakup region. The corresponding breakup features are exemplified by the case at S = 2.1 in Fig. 7. The deformation of the lead droplet progresses in a conventional manner until T = 1.7 when the collision with the trailing droplet triggers an early rupture of the inflating bag. In terms of the trailing droplet, the deformation starts with weakened flattening (T = 0.7). As the lead droplet deforms into a thin disk, the trailing droplet suffers from stronger shielding effects and consequently enters a contraction period. The trailing droplet contracts into a triangular shape pointing upstream at T = 1.2 and further into an ellipsoid with the major axis aligned with the streamwise direction at T = 1.7. The ellipsoidal trailing droplet punctures the bag structure of the lead droplet at T^* = 2.0 and escapes from its shelter. Being exposed to the freestream flow, the trailing droplet gets flattened at the windward surface and distorted into a "T" shape at T^* = 2.5. In the following period, the droplet fails to reproduce the typical bag breakup, but tends to disintegrate into several fragments of comparable sizes to the original.

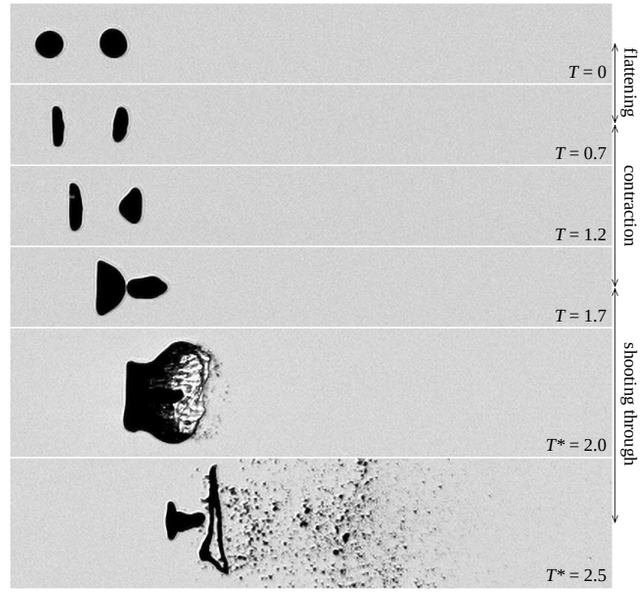

Fig. 7. Puncture of the bag structure of the lead droplet by the trailing droplet (S = 2.1, We = 14).

3.1.3 Suppressed breakup region: coalescence of the tandem droplets

The case at S = 1.2 in the suppressed breakup region exhibits new features as presented in Fig. 8 and is categorized as the coalescence mode. The most noticeable feature is the absence of bag structures. The early-stage flattening of the lead droplet

is maintained, while the deformation of the trailing droplet starts with streamwise stretching. The disk-shape lead droplet and the teardrop-shape trailing droplet (T = 1.0) coalesce into a funnel shape at T = 1.35. The coalescence is completed around T = 1.7 when the tail of the trailing droplet is swallowed entirely. In the later stage, the deformation of the merged body becomes highly disordered. Apart from the formation and fragmentation of ligament structures (T^* = 2.8), the main body tends to split into large children droplets. This coalescence mode and the afore-mentioned puncture mode have also been observed by Zhao et al. (2019) for separation distances below and above 1.3 respectively, with which our present results are in good consistency.

To better explain how the shielding effect changes the early-stage deformation of the trailing droplet from cross-stream flattening to streamwise stretching, Fig. 9 presents a simplified 2D sketch of streamlines around two closely packed droplets. The red circles represent stagnation points with the highest static pressure along the droplet surface, and the blue circles correspond to those with relatively lower pressure. With the presence of the lead droplet, the highest pressure at the trailing droplet surface appears at locations near the equator. The resulting pressure imbalance extrudes a sharp nose at the droplet front (T = 0.35 in Fig. 8) and results in the following streamwise stretching (T = 0.7 in Fig. 8).

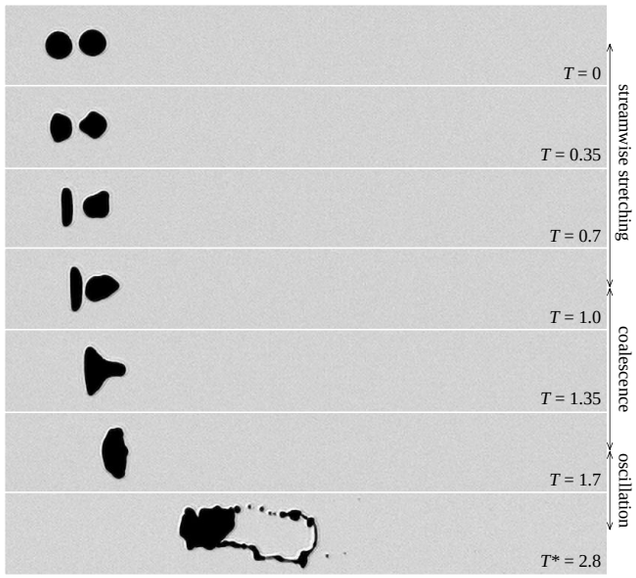

Fig. 8. Coalescence of lead and trailing droplets (S = 1.2, We = 13).

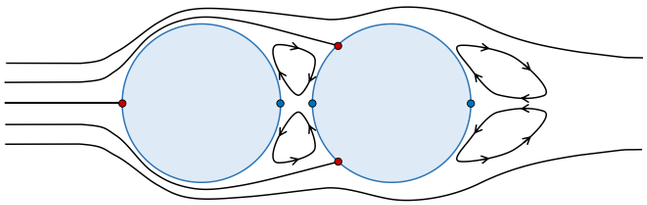

Fig. 9. Simplified 2D sketch of streamlines around tandem droplets at S = 1.2. Stagnation points of the highest static pressure are labelled in red and those of low pressure in blue.

In summary, the presence of the lead droplet tends to weaken the bag inflation of the trailing droplet. This reduces the production of fine mist through bag rupture and favors the generation of large fragments. For a more accurate modelling of the fragment size distribution, special attention needs to be paid to cases where the trailing droplet fails to follow bag breakup and produces fragments with sizes comparable to the initial diameter.

3.2 Bag-and-stamen breakup

3.2.1 Transition region: smaller bag for the trailing droplet

For the bag-and-stamen breakup, the transition region covers experiments with separation distances from S = 3.7 to 8.0 in the current study. An exemplary case is shown in Fig. 10 with S = 8.0 and We = 25. During the initial flattening, a bulge forms at the frontal surface of the lead droplet, marking the development of a stamen (T = 1.0). After the bag inflates around the stamen to the maximum size, the bag rupture, the ring fragmentation and the stamen disintegration take place in succession. The trailing droplet shares similar breakup features except that it deforms at a slower rate and develops a smaller bag.

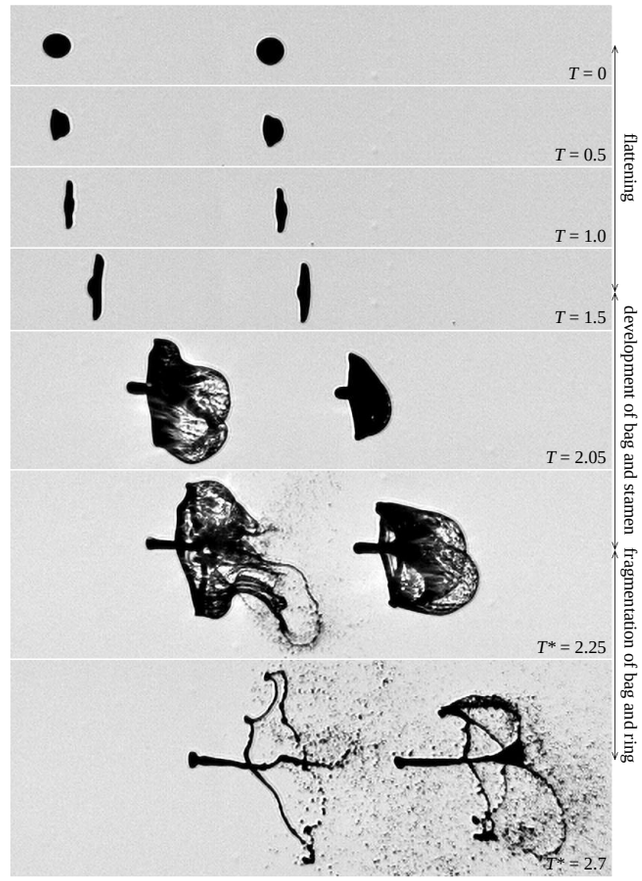

Fig. 10. Weaker flattening and smaller bag size for the trailing droplet under the shielding effect of the lead droplet (S = 8.0, We = 25).

Fig. 11 compares the variation of the bag size (top row) and the ring/stamen thickness (bottom row) of the trailing droplet among cases in the transition region. Although detailed breakup structures are considerably distorted by the shielding effect of the lead droplet, main bag-and-stamen breakup features are still maintained. Nevertheless, the bag of the trailing droplet shrinks and the ring/stamen structures are thickened as the separation distance decreases, which is similar to the observations for bag breakup in Fig. 6.

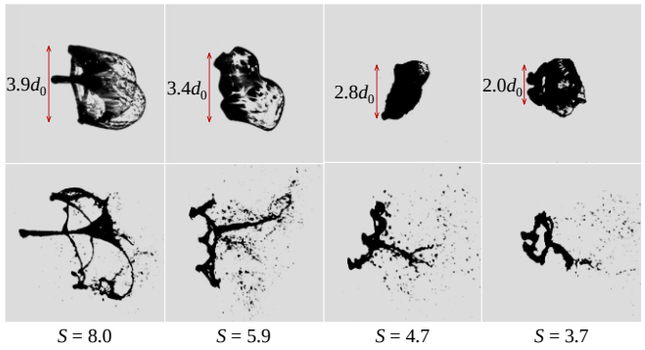

Fig. 11. Variation of the bag size and the ring/stamen thickness at different separation distances for the trailing droplet in the bag-and-stamen breakup regime. The top and bottom rows correspond to time instants prior and subsequent to the bag rupture, respectively. (We = 25, 22, 25 and 24 from left to right).

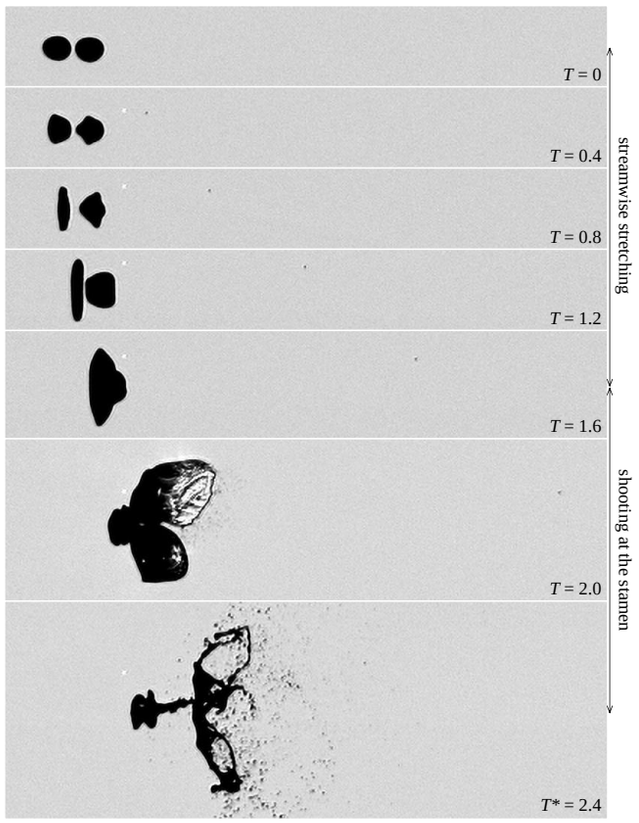

Fig. 12. Puncture of the bag structure of the lead droplet and coalescence of the trailing droplet with the stamen (S = 1.2, We = 24).

3.2.2 Suppressed breakup region: puncture of the lead droplet by the trailing droplet

The two cases with the closest separation distances S = 1.2 and 2.0 lie in the suppressed breakup region, where the lead droplet collides with the trailing droplet during the early development of bag structures as shown in Fig. 12. The shielding effect on the trailing droplet is clearly observed at the very beginning of the deformation. In contrast to the conventional cross-stream flattening, the trailing droplet deforms into an arrowhead shape at T = 0.8 and later together with the flattened lead droplet constitutes a mushroom shape (T = 1.2). This mushroom layout has also been reported in the numerical work by Quan et al. (2011) at We between 4 and 40 and S = 1.6 which falls between the separation distances of the two present cases in the suppressed breakup region. At T = 2.0, the trailing droplet punctures the bag structure of the lead droplet and coalesces with its stamen. The ligament that stretches at the rear of the intact trailing droplet at T* = 2.4 resembles the conventional stamen. In the subsequent period, apart from formation of small bags, the main body of the trailing droplet tends to disintegrate into large pieces.

Overall speaking, the influence of the lead droplet on the breakup behavior of the trailing droplet in the bag-and-stamen morphology is similar to that in the bag breakup morphology. The bag development of the trailing droplet is weakened and more mass is preserved in the ring/stamen structure or in an intact body. Consequently, a larger portion of the trailing droplet is atomized into large fragments instead of fine mist.

3.3 Multibag breakup

3.3.1 Transition region: dampened bag formation

For the multibag breakup, the transition region covers the current cases with separation distances from S = 1.9 to 6.2. The breakup behavior of the tandem droplets is characterized in Fig. 13 with the case at S = 6.2 and We = 68. The deformation of the lead droplet starts with the typical flattening (T = 1.0), followed by a short period of bending of the thin peripheral sheet (T = 1.45). Then, consecutive formation and rupture of bags take place around the periphery, shedding small mist into the flow (T = 1.85). The remaining stamen-like structure at T = 2.6 further fragments through rupture of tiny bags and fracture of thin ligaments. The trailing droplet follows the breakup morphology of the lead droplet, but the formation and rupture of bags are noticeably dampened by the shielding effect. Compared to the bag-and-stamen breakup, the multibag mode leaves a thicker stamen-like structure and generates no toroidal ring.

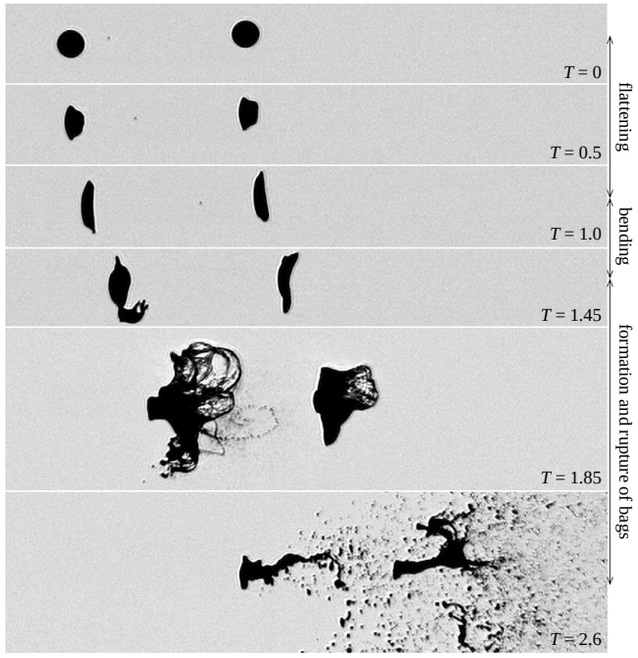

Fig. 13. Less intense formation of bags for the trailing droplet under the shielding effect of the lead droplet (S = 6.2, We = 68).

3.3.2 Suppressed breakup region: coalescence of the trailing droplet with the stamen-like structure of the lead droplet

When the separation distance drops to 1.2, the lead droplet still maintains main features of the multibag morphology, but the breakup of the trailing droplet is significantly altered as shown in Fig. 14. The strong shielding effect shapes the front

of the trailing droplet into a sharp cone (T = 0.4). A liquid sheet is subsequently developed along the periphery (T = 0.7) and stretched in the streamwise direction (T = 1.0). The elongated trailing droplet collides with the flattened lead droplet at T = 1.4 and coalesces into the stamen-like structure that emerges at T = 2.6.

In the multibag morphology, the burst of bags of the lead droplet tends to eject fine fragments widely in the cross-stream direction. However, since the bag inflation of the trailing droplet is significantly dampened by the shielding effect as shown in Fig. 13, the resultant fragments gain less cross-stream momentum from the outward splash of the bag rupture and thus the spatial distribution is substantially confined. After the tandem droplets collide and merge, their fragments are blended together and dispersed in a conical pattern. Fig. 15 compares the dispersion angle of the mixed fragments at T = 3.0, and shows that the dispersion angle is narrowed from 81° to 59° as the separation distance decreases from 3.8 to 1.2.

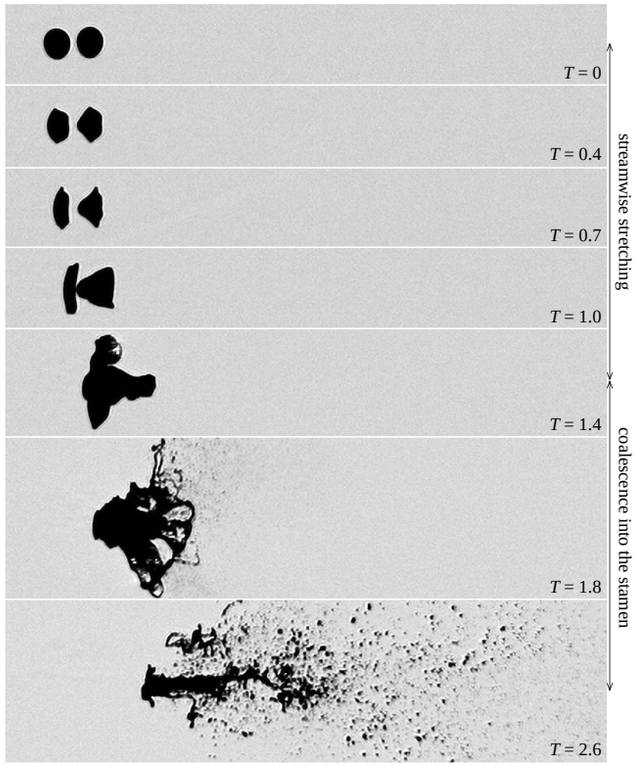

Fig. 14. Coalescence of the trailing droplet into the stamen-like structure of the lead droplet (S = 1.2, We = 68).

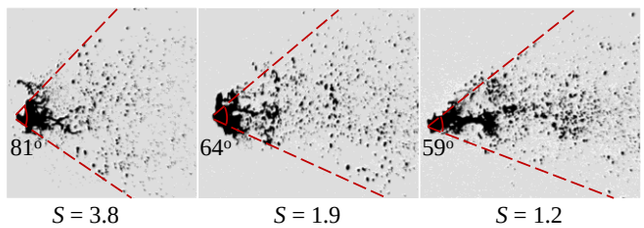

Fig. 15. Dispersion angle of the fragments detaching from the merged body of the tandem droplets in the multibag regime at T = 3.0. (We = 68, 70 and 68 from left to right).

3.4 Shear stripping

3.4.1 Transition region: narrower fragment dispersion for the trailing droplet

The last morphology covered in the current work is the shear stripping breakup, which is also conventionally understood as the ultimate breakup regime (Theofanous and Li 2008). The transition region for this breakup morphology covers all present cases with $S \leq 4.5$ and no suppressed breakup region is identified in the current work. Fig. 16 shows the exemplary case with S = 3.8 and We = 179. The lead and trailing droplets share the same breakup morphology, consisting of initial flattening (T = 0.3), bending of the peripheral sheet (T = 0.6) and stripping of fine mist along the sheet (T = 1.2). The breakup is characterized by the fragmentation of the peripheral sheet into thin ligaments and further into micro-droplets. Consecutive inflation and burst of tiny bags along the peripheral sheet is observed at the very beginning of the fragmentation (T = 0.85) but ceases in a short time. The main difference between the tandem droplets is that in the late stage the trailing droplet is less flattened and the resultant fragments are dispersed less widely in the cross-stream direction. Igra and Takayama (2003) have reported similar observations for tandem water columns separated at S = 5 for a much higher Weber number of 6900.

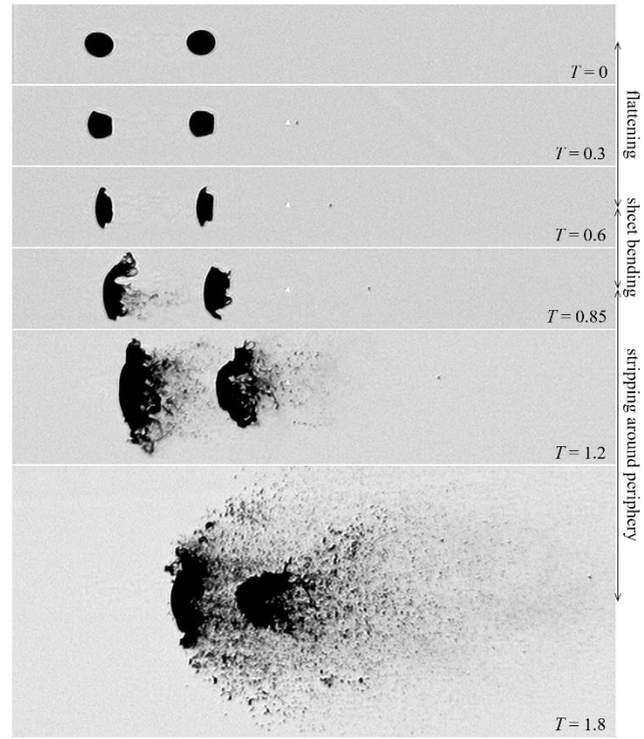

Fig. 16. Narrower cross-stream dispersion of the trailing droplet fragments under the shielding effect of the lead droplet (S = 3.8, We = 179).

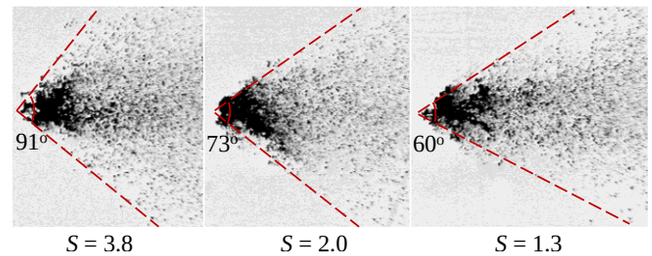

Fig. 17. Dispersion angle of the fragments detaching from the merged body of the tandem droplets in the shear stripping regime at T = 3.0. (We = 179, 183 and 184 from left to right).

It is worth mentioning that at the smallest separation distance S = 1.3 in the present study, the trailing droplet is shaped with a sharply tapered front similarly to that shown in

Fig. 14 in the early stage but follows main stripping breakup features afterwards. The corresponding image sequence is omitted for brevity.

Fig. 17 compares the dispersion angle of fragments shed off the merged body of the tandem droplets at T = 3.0 for cases at S = 3.8, 2.0 and 1.3. The cross-stream span occupied by the fragments becomes consistently narrower as the separation distance decreases. This trend is consistent with that observed in Fig. 15 for the multibag regime.

3.5 Quantitative analyses of the early-stage deformation of the tandem droplets

The early-stage deformation of droplets plays a crucial role in determining the subsequent breakup morphology, and the associated parameters are also of practical importance for numerical validations. This section quantifies the early-stage behavior of the tandem droplets and highlights the variation at different Weber numbers and separations distances. The quantified parameters in the current work are the time of initial deformation T_{ini}, the maximum cross-stream diameter D_{cmax} and the mean drag coefficient C_{dmean}.

The initial deformation of droplets ends at the time instant of the minimum streamwise diameter. This time instant T_{ini} marks the start of the bag inflation for bag and bag-and-stamen morphologies and the bending of the peripheral sheet over the rear surface for multibag and shear stripping morphologies. The definition was proposed by Pilch and Erdman (1987) to indicate the breakup initiation and also adopted in other literature (Hsiang and Faeth 1992; Guildenbecher, López-Rivera, and Sojka 2009). The maximum cross-stream diameter D_{cmax} is the cross-stream diameter at T_{ini} normalized against the initial diameter. The mean drag coefficient C_{dmean} is calculated by fitting the streamwise displacement of the droplet mass center x_{mc} between T = 0 and T_{ini} into the relation

$$x_{mc} / d_0 = 3 / 8 \cdot C_{dmean} T^2 \qquad \textbf{(Eqn. 5)}$$

derived by Ranger and Nicholls (1969). For all cases T_{ini} lies within the steady-flow time window.

3.5.1 Influence of the tandem formation on the early-stage deformation of the lead droplet

Table 2 summarizes T_{ini}, D_{cmax} and C_{dmean} of the lead droplet in different breakup morphologies. The values are averaged from experiments of which the breakup regime is the same but the separation distances are varied. The time of initial deformation $T_{ini,lead}$ decreases consistently from 1.19 at We = 13 to 0.71 at We = 180. This tendency is in agreement with the empirical correlation

$$T_{ini} = 1.9(We\text{-}12)^{-0.25}\left(1+2.2Oh^{1.6}\right) \qquad \textbf{(Eqn. 6)}$$

proposed by Pilch and Erdman (1987), except that this correlation predicts a higher value of 1.9 at We = 13. Meanwhile, the maximum cross-stream diameter $D_{cmax,lead}$ peaks with the value of 1.88 for bag-and-stamen breakup and then declines as We keeps increasing. The data points reported by Zhao et al. (2010) show the same trend but slightly different magnitudes. In terms of the mean drag coefficient $C_{dmean,lead}$, the effect of the droplet flattening is not excluded in the current calculation. Consequently, in addition to flow Reynolds numbers, $C_{dmean,lead}$ is also significantly influenced by the growth rate of the droplet cross-stream diameter. This explains the observation that $C_{dmean,lead}$ follows a similar trend to $D_{cmax,lead}$ and that the magnitudes exceed 1.2 which is the drag coefficient of a circular disk (Roos and Willmarth 1971). Overall speaking, the early-stage behavior of the lead droplet is barely influenced by the tandem formation and the quantified parameters are consistent with those of isolated droplets.

Table 2. The time of initial deformation T_{ini}, the maximum cross-stream diameter D_{cmax} and the mean drag coefficient C_{dmean} of the lead droplet, averaged from experiments in the same breakup morphology.

We	$T_{ini,lead}$	$D_{cmax,lead}$	$C_{dmean,lead}$
13 (±1.3)	1.19 (±1.2%)	1.67 (±3.6%)	1.40 (±1.4%)
24 (±2.2)	1.08 (±1.7%)	1.88 (±3.9%)	1.58 (±2.1%)
70 (±3.0)	0.83 (±2.3%)	1.73 (±4.2%)	1.25 (±3.0%)
180 (±10)	0.71 (±2.4%)	1.67 (±4.4%)	1.20 (±2.3%)

Table 2 also provides the range of variation for T_{ini}, D_{cmax} and C_{dmean}. All three parameters vary within the interval of ±4.5%. The variation is mainly caused by the difference in the flow conditions (which is also implied by the variation of Weber numbers) and the irregularity of the initial droplet shapes. Compared to the overall variation, the measurement uncertainty is relatively low. With current framing rates and spatial resolutions of the recorded images, the uncertainty for temporal and spatial calculations is ±1.3% and ±1.5%, respectively.

3.5.2 Influence of the tandem formation on the early-stage deformation of the trailing droplet

This section is focused on the influence of the tandem formation on the breakup behavior of the trailing droplet. The *S*-*We* maps of the time of initial deformation, the maximum cross-stream diameter and the mean drag coefficient are presented sequentially. Considering that the lead and trailing droplets from one experiment experience identical flow conditions and tend to share similar initial shapes, the data points presented for the trailing droplet are normalized against values of the lead droplet, in order to minimize the uncertainties brought by flow variation and shape irregularity.

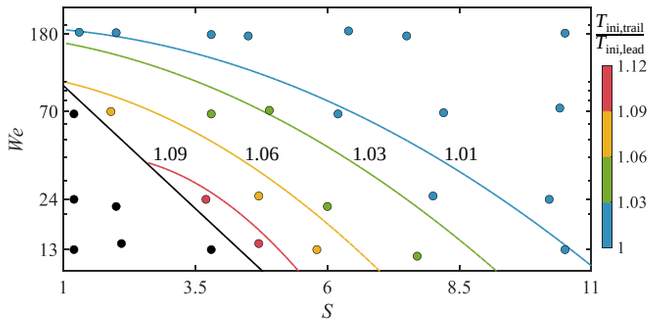

Fig. 18. Time of initial deformation of the trailing droplet at different separation distances and Weber numbers, normalized by values of the lead droplet.

The time of initial deformation of the trailing droplet relative to the lead droplet $T_{ini,trail}/T_{ini,lead}$ is plotted in Fig. 18 over the *S*-*We* map. Isolines of 1.01, 1.03, 1.06 and 1.09 provided in the figure are calculated through interpolation of the discrete data points. Cases in the suppressed breakup region are labelled as dark circles and excluded in the present calculation since the trailing droplet fails to initiate the breakup independently. Generally speaking, $T_{ini,trail}$ is postponed by the tandem formation and the postponement is longer at smaller S and lower We. For low-We bag and bag-and-stamen morphologies, T_{ini} is marked by the end of droplet flattening. The flattening is caused by the pressure imbalance around the droplet and highly sensitive to the shielding effect which significantly reduces the pressure imposed on the front of the trailing droplet as illustrated in Fig. 9. For high-We multibag

and shear stripping morphologies, however, T_{ini} is indicated by the bending of the peripheral sheet over the droplet rear. As demonstrated by the experimental work of Theofanous et al. (2012) and Wang et al. (2020), development of the peripheral sheet is dominated by the local shear flow around the equator which is much less influenced by the shielding effect than the pressure imbalance around the droplet. Consequently, the postponement of $T_{ini,trail}$ is strongly reduced as the Weber number increases. Particularly, the influence is negligible in the shear stripping regime.

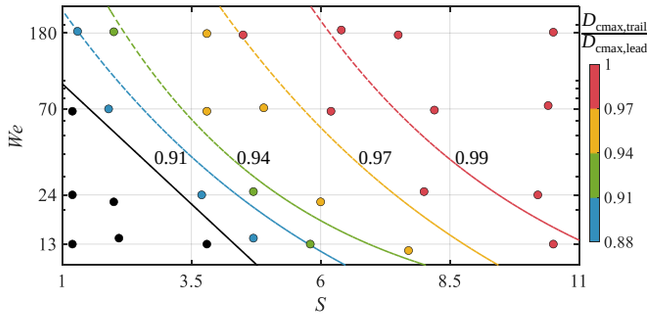

Fig. 19. Maximum cross-stream diameter of the trailing droplet at different separation distances and Weber numbers, normalized by values of the lead droplet.

Fig. 19 presents the maximum cross-stream diameter of the trailing droplet normalized against values of the lead droplet $D_{cmax,trail}/D_{cmax,lead}$. Interpolated isolines of 0.99, 0.97, 0.94 and 0.91 are also displayed. The general tendency is that $D_{cmax,trail}$ is reduced by the presence of the lead droplet and the reduction is higher at closer S and lower We. For all breakup morphologies, the growth of the cross-stream diameter is dominated by the flattening of the main body. As discussed before, the shielding effect of the lead droplet reduces the pressure at the front of the trailing droplet and thus results in lower $D_{cmax,trail}$. The strength of the shielding effect differs from case to case. The lead droplet deforms into a flat disk at low We (T = 1.0 in Fig. 5) and into an ellipsoid at high We (T = 0.6 in Fig. 16). Ellipsoidal shapes induce weaker flow separation in the wake than flat disks and the corresponding shielding is less effective. In addition, the cross-stream diameter of the deformed lead droplet tends to be smaller at higher We, which further alleviates the shielding effect on the trailing droplet. Consequently, the reduction of $D_{cmax,trail}$ is lowered as the Weber number increases.

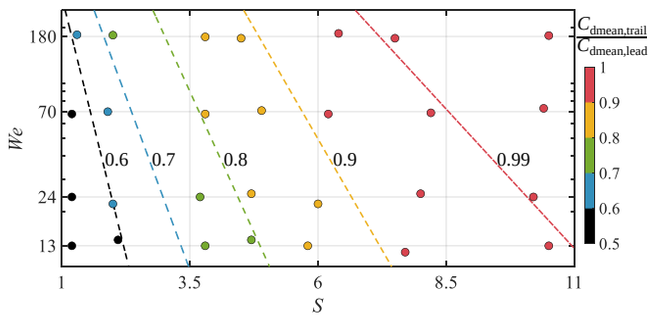

Fig. 20. Mean drag coefficient of the trailing droplet at different separation distances and Weber numbers, normalized by values of the lead droplet.

The variation of the mean drag coefficient of the trailing droplet over the S-We map is shown in Fig. 20. For cases where the trailing droplet fails to initiate the breakup independently, $C_{dmean,trail}$ is calculated by fitting into Eqn. 5 the data prior to the collision with the lead droplet. The change of $C_{dmean,trail}$ with S and We follows similar patterns to $D_{cmax,trail}$. Again, the shielding effect is stronger at smaller S and lower We and accounts for the reduction of $C_{dmean,trail}$.

4 Summary and Conclusion

The present work experimentally investigates the breakup of two identically-sized droplets in tandem formation. The breakup is triggered by a planar shock wave and recorded by an ultra-high-speed camera integrated into a shadowgraph system. The experimental matrix consists of seven separation distances S ranging from 1.2 to 10.5 times of the droplet diameter and four Weber numbers We between 13 and 180 covering bag, bag-and-stamen, multibag and shear stripping breakup morphologies. The influences of the tandem formation on the breakup behavior are summarized as follows.

(a) The presence of the trailing droplet exerts marginal effects on the lead droplet. The lead droplet replicates the breakup morphology of isolated droplets in all cases, except for the bag breakup at S = 1.2 where the tandem droplets coalesce with no further bag formation.

(b) When the separation distance falls below critical levels, the breakup intensity of the trailing droplet is consistently weakened although the conventional breakup morphology is preserved. In the early stage, the tandem formation postpones the time of initial deformation for the trailing droplet, lowers the maximum cross-stream diameter and reduces the mean drag coefficient. These effects are stronger at lower Weber numbers and are intensified as the separation distance decreases. In the late stage, the bag structure is inflated to a smaller size for bag and bag-and-stamen morphologies and the fragments are less widely dispersed in the cross-stream direction for multibag and shear stripping morphologies. Notably, the critical separation distance is We-dependent and halved from S = 10.8 at We = 13 to S = 5.4 at We = 180.

(c) For cases where the tandem droplets are in very close proximity, the trailing droplet exhibits streamwise stretching instead of flattening during the initial deformation and either punctures or coalesces with the lead droplet in the later period.

To the best of our knowledge, the current study is the first work that experimentally investigates tandem droplet breakup over a wide range of Weber numbers and separation distances. The present results can be particularly helpful for accurate modelling of fragment sizes and breakup timings in applications related with dense sprays.

Acknowledgement

The authors acknowledge funding by the European Research Council (ERC) under the European Union's Horizon 2020 research and innovation program (grant agreement No. 667483).

Data Availability Statement

The data that support the findings of this study are openly available in mediaTUM.

References

[1] Ashgriz, N. 2011. *Handbook of Atomization and Sprays: Theory and Applications*. Springer Science & Business Media.

[2] Chen, Y., E. P. DeMauro, J. L. Wagner, M. Arienti, D. R. Guildenbecher, P. Farias, T. W. Grasser, et al. 2017. "Aerodynamic Breakup and Secondary Drop Formation for a Liquid Metal Column in

a Shock-Induced Cross-Flow." In *55th AIAA Aerospace Sciences Meeting*, 1–15. Reston, Virginia: American Institute of Aeronautics and Astronautics.

[3] Chiang, C. H., and W. A. Sirignano. 1993. "Axisymmetric Calculations of Three-Droplet Interactions." *Atomization and Sprays* 3 (1).

[4] Chou, W. H., and G. M. Faeth. 1998. "Temporal Properties of Secondary Drop Breakup in the Bag Breakup Regime." *International Journal of Multiphase Flow* 24 (6): 889–912.

[5] Dai, Z., and G. M. Faeth. 2001. "Temporal Properties of Secondary Drop Breakup in the Multimode Breakup Regime." *International Journal of Multiphase Flow* 27 (2): 217–36.

[6] Dorr, G. J., A. J. Hewitt, S. W. Adkins, J. Hanan, H. Zhang, and B. Noller. 2013. "A Comparison of Initial Spray Characteristics Produced by Agricultural Nozzles." *Crop Protection* 53: 109–17.

[7] Faeth, G. M., L. P. Hsiang, and P. K. Wu. 1995. "Structure and Breakup Properties of Sprays." *International Journal of Multiphase Flow* 21: 99–127.

[8] Guildenbecher, D. R., C. López-Rivera, and P. E. Sojka. 2009. "Secondary Atomization." *Experiments in Fluids* 46 (3): 371–402.

[9] Han, J., and G. Tryggvason. 1999. "Secondary Breakup of Axisymmetric Liquid Drops. I. Acceleration by a Constant Body Force; Mechanics of Air-Assisted Liquid Atomization." *Atomization Sprays* 11; 3 (12): 3650; 55–3667.

[10] Hinze, J. O. 1955. "Fundamentals of the Hydrodynamic Mechanism of Splitting in Dispersion Processes." *AIChE Journal* 1 (3): 289–95.

[11] Hsiang, L. P., and G. M. Faeth. 1992. "Near-Limit Drop Deformation and Secondary Breakup." *International Journal of Multiphase Flow* 18 (5): 635–52.

[12] Igra, D., and K. Takayama. 2003. "Experimental Investigation of Two Cylindrical Water Columns Subjected to Planar Shock Wave Loading." *Journal of Fluids Engineering* 125 (2): 325.

[13] Jain, M., R. S. Prakash, G. Tomar, and R. V. Ravikrishna. 2015. "Secondary Breakup of a Drop at Moderate Weber Numbers." *Proceedings of the Royal Society A: Mathematical, Physical and Engineering Sciences* 471 (2177).

[14] Joseph, D. D., J. Belanger, and G. Beavers. 1999. "Breakup of a Liquid Drop Suddenly Exposed to a High Speed Airstream." *International Journal of Multiphase Flow* 25: 1263–1303.

[15] Kékesi, T., M. Altimira, G. Amberg, and L. Prahl Wittberg. 2019. "Interaction between Two Deforming Liquid Drops in Tandem and Various Off-Axis Arrangements Subject to Uniform Flow." *International Journal of Multiphase Flow* 112: 193–218.

[16] Kim, J., J. K. Lee, and K. M. Lee. 2016. "Accurate Image Super-Resolution Using Very Deep Convolutional Networks." In *2016 IEEE Conference on Computer Vision and Pattern Recognition (CVPR)*, 1646–54. IEEE.

[17] Lagutkin, S., L. Achelis, S. Sheikhaliev, V. Uhlenwinkel, and V. Srivastava. 2004. "Atomization Process for Metal Powder." *Materials Science and Engineering A* 383 (1 SPEC. ISS.): 1–6.

[18] Lane, W. R. 1951. "Shatter of Drops in Streams of Air." *Industrial & Engineering Chemistry* 43 (6): 1312–17.

[19] Liu, D. Y., K. Anders, and A. Frohn. 1988. "Drag Coefficients of Single Droplets Moving in an Infinite Droplet Chain on the Axis of a Tube." *International Journal of Multiphase Flow* 14 (2): 217–32.

[20] Liu, Z., and R. D. Reitz. 1997. "An Analysis of the Distortion and Breakup Mechanisms of High Speed Liquid Drops." *International Journal of Multiphase Flow* 23 (4): 631–50.

[21] Mostaghimi, J., M. Pasandideh-Fard, and S. Chandra. 2002. "Dynamics of Splat Formation in Plasma Spray Coating Process." *Plasma Chemistry and Plasma Processing* 22 (1): 59–84.

[22] Mulholland, J. A., R. K. Srivastava, and J. O. L. Wendt. 1988. "Influence of Droplet Spacing on Drag Coefficient in Nonevaporating, Monodisperse Streams." *AIAA Journal* 26 (10): 1231–37.

[23] Nguyen, Q. V., and D. Dunn-Rankin. 1992. "Experiments Examining Drag in Linear Droplet Packets." *Experiments in Fluids* 165: 157–65.

[24] Pilch, M., and C. A. Erdman. 1987. "Use of Breakup Time Data and Velocity History Data to Predict the Maximum Size of Stable Fragments for Acceleration-Induced Breakup of a Liquid Drop." *International Journal of Multiphase Flow* 13 (6): 741–57.

[25] Poo, J. Y., and N. Ashgriz. 1991. "Variation of Drag Coefficients in an Interacting Drop Stream." *Experiments in Fluids* 11 (1): 1–8.

[26] Quan, S., J. Lou, and H. A. Stone. 2011. "Interactions between Two Deformable Droplets in Tandem Subjected to Impulsive Acceleration by Surrounding Flows." *Journal of Fluid Mechanics* 684: 384–406.

[27] Ranger, A. A., and J. A. Nicholls. 1969. "Aerodynamic Shattering of Liquid Drops." *AIAA Journal* 7 (2): 285–90.

[28] Reitz, R. D., and R. Diwakar. 1986. "Effect of Drop Breakup on Fuel Sprays." *SAE Technical Paper Series* 1.

[29] Roos, F. W., and W. W. Willmarth. 1971. "Some Experimental Results on Sphere and Disk Drag." *AIAA Journal* 9 (2): 285–91.

[30] Stefanitsis, D., I. Malgarinos, G. Strotos, N. Nikolopoulos, E. Kakaras, and M. Gavaises. 2019. "Numerical Investigation of the Aerodynamic Breakup of Droplets in Tandem." *International Journal of Multiphase Flow* 113: 289–303.

[31] Temkin, S., and G. Z. Ecker. 1989. *Droplet Pair Interactions in a Shock-Wave Flow Field. Journal of Fluid Mechanics*. Vol. 202.

[32] Theofanous, T. G., and G. J. Li. 2008. "On the Physics of Aerobreakup." *Physics of Fluids* 20 (5).

[33] Theofanous, T. G., G. J. Li, and T. N. Dinh. 2004. "Aerobreakup in Rarefied Supersonic Gas Flows." *Journal of Fluids Engineering* 126 (4): 516.

[34] Theofanous, T. G., V. V. Mitkin, C. L. Ng, C-H. Chang, X. Deng, and S. Sushchikh. 2012. "The Physics of Aerobreakup. II. Viscous Liquids." *Physics of Fluids* 24 (2): 022104.

[35] Wang, Z., T. Hopfes, M. Giglmaier, and N. A Adams. 2020. "Effect of Mach Number on Droplet Aerobreakup in Shear Stripping Regime." *Experiments in Fluids* 61 (9): 1–17.

[36] Zhao, H., H. Liu, W. Li, and J. Xu. 2010. "Morphological Classification of Low Viscosity Drop Bag Breakup in a Continuous Air Jet Stream." *Physics of Fluids* 22 (November 2010).

[37] Zhao, H., Z. Wu, W. Li, J. Xu, and H. Liu. 2019. "Interaction of Two Drops in the Bag Breakup Regime by a Continuous Air Jet." *Fuel* 236 (April 2018): 843–50.